

Original Article

Preparation of C_3N_4 quantum dots sensitized Iron MOF composites to photocatalytically degrade congo red solution

Changbo Zhang^a, Junjie Bai^b, Liang Wu^c, Tong Lv^d, Shunshun Yu^d, Yuguo Zheng^a, Zhenyu Shi^a, Bingke Li^d, Keliang Wu^{d,*}

^aDepartment of School of Biology and Chemistry, Minzu Normal University of Xingyi, Xingyi, China

^bDepartment of Petroleum and Chemical, Bayinguoleng Vocational and Technical College, Kurlu, Xinjiang, China

^cZhejiang Jusheng Fluorine Chemistry Co., Ltd, Quzhou, Zhejiang, China

^dDepartment of School of Biology and Chemical Engineering, Nanyang Institute of Technology, Nanyang, Henan, China

ARTICLE INFO

Keyword:

Charge separation efficiency
Dye wastewater treatment
MIL-101(Fe)
Photocatalytic degradation

ABSTRACT

MIL-101(Fe), despite its high surface area and adsorption capacity, suffers from rapid electron-hole recombination that limits photocatalytic efficiency. To overcome this challenge, we engineered a C_3N_4 quantum dots (QDs) /MIL-101(Fe) composite via a facile loading method. Comprehensive characterization by X-ray diffraction (XRD), transmission electron microscopy (TEM), X-ray photoelectron spectroscopy (XPS), Brunauer-Emmett-Teller (BET) verified the effective incorporation of C_3N_4 QDs, which significantly suppressed charge carrier recombination and enhanced visible-light harvesting. The optimized composite demonstrated superior photocatalytic performance, achieving near-complete degradation of 100 mg/L Congo red within 20 mins under visible light, far exceeding the activity of pristine MIL-101(Fe). This study provides a rational design strategy to improve charge separation in metal-organic framework-based photocatalysts for organic pollutant remediation.

1. Introduction

Growing industrialization has led to the wide discharge of many organic pollutants into the environment, posing a serious threat to human health and ecosystems. These pollutants are bioaccumulative and can spread through the food chain, causing a variety of health problems [1-3]. Moreover, they do not easily degrade under natural conditions, and their long-term presence in the environment can disrupt the ecological balance of various ecosystems [4,5]. Existing chemical and physical methods used for the treatment of organic pollutants often have problems, such as high costs, low efficiency, and the easy generation of secondary pollutants [6-8]. In comparison, photocatalytic degradation technology is highly efficient and offers good environmental protection characteristics. Photocatalytic degradation methods involve the photogeneration of holes and electrons by a photocatalyst under light conditions. Consequently, redox reactions occur with organic pollutants, leading to the decomposition of the pollutants into harmless small molecules [9-11]. In this process, the selection of the photocatalyst and the optimization of reaction conditions are key factors for achieving good performance [12-15].

In recent years, many important achievements and breakthroughs have been made in the field of photocatalytic degradation, providing strong support for practical applications. [16-18] Increasingly, photocatalytic research is focused on improving the activity, stability, and selectivity of photocatalysts as well as exploring more efficient reaction systems and conditions [19-21]. Metal-organic frameworks (MOFs) are particularly compelling photocatalytic materials. These

crystalline materials contain highly uniform pore structures formed by interconnecting metal ions and organic ligands. Because they have controllable structures, large surface areas, and high porosities, MOF materials have been widely used for the treatment of organic pollutants in recent years [22-24]. However, MOF materials exhibit drawbacks such as poor material stability and low photogenerated electron separation and transfer efficiency that have limited their practical application [25,26]. Therefore, modifying MOF materials to obtain better performance is of great significance.

Quantum dots (QDs) are a category of nanoparticles that have strong quantum confinement and boundary effects, as well as superior optical properties. Thus, QDs show great promise for photocatalytic applications [27-29]. C_3N_4 QDs are non-metallic semiconductors that can be used as visible-light-induced photocatalysts. These QDs have an abundance of surface functional groups, good dispersion, high chemical stability, a 2.7 eV band gap, and large specific surface areas [30-32]. Moreover, they are capable of strongly absorbing visible light at wavelengths up to 450 nm. The unique triazine ring or tri-S-triazine ring structure of C_3N_4 QDs provides good thermal stability as well as good acid and alkali resistance. Thus, the use of C_3N_4 QDs for CO_2 reduction, pollutant degradation, and other applications has been widely investigated [33-35].

MIL-101(Fe) exhibits advantageous structural properties, high surface area, and strong adsorption capacity, making it a promising photocatalyst [36]. However, its practical application is limited by rapid electron-hole recombination and low charge utilization efficiency [37-39]. To address these limitations, we propose a rational interface

*Corresponding author:

E-mail address: wukeliang@nyist.edu.cn (K. Wu)

Received: 20 December, 2024 Accepted: 09 April, 2025 Epub Ahead of Print: 18 June 2025 Published: ***

DOI: 10.25259/AJC_296_2024

engineering strategy integrating C_3N_4 QDs, known for their exceptional light-harvesting and charge-transfer capabilities, onto MIL-101(Fe) to construct a heterojunction system [40]. The primary aim of this work is to elucidate the synergistic mechanism between C_3N_4 QDs and MIL-101(Fe) and to establish a structure-activity relationship for enhanced photocatalytic degradation of organic pollutants. Herein, we report a facile hydrothermal synthesis of C_3N_4 QDs/MIL-101(Fe) composites. The optimized composite achieves a 99.5% degradation efficiency for Congo red within 20 mins under simulated solar light, attributed to significantly suppressed charge recombination and improved electron utilization kinetics. This study provides fundamental insights into MOF-based heterostructure design for environmental remediation.

2. Materials and Methods

2.1. Materials and characterization

N, N-dimethylformamide (DMF, C_3H_7NO , 99.5%) was provided by Tianjin Fuchen Chemical Reagent Factory. Iron (III) chloride hexahydrate ($FeCl_3 \cdot 6H_2O$, 99%), urea (CH_4N_2O , 99%), 2-aminoterephthalate ($C_8H_7NO_4$, 98%), and trisodium citrate ($C_6H_5Na_3O_7$, 99%) were acquired from Shanghai Macklin Biochemical Co., Ltd. Anhydrous ethanol (CH_3COOH , 99.5%) and anhydrous disodium sulfate (Na_2SO_4 , 99%) were acquired from Sinopharm Chemical Reagent Co., Ltd. Water was deionized for all experiments, and all chemicals were of analytical purity.

X-ray diffraction (XRD) was performed with a MiniFlex600 to evaluate crystal structures. Morphologies were studied using transmission electron microscopy (TEM) (JEOL JEM-2100PLUS, Nippon Electronics Co., LTD.) and scanning electron microscopy (SEM) (JEOL JSM-7900F, Nippon Electronics Co., LTD.). Textural characteristics were studied using an SSA-4300 (Beijing Biode Electronic Technology Co., Ltd.) to perform nitrogen adsorption-desorption analysis. UV-visible diffuse reflectance spectroscopy (UV-vis DRS) was performed with aUV-2450 (Shimadzu Co., Ltd.) to evaluate molecular structures. A CHI760E electrochemical workstation manufactured by Shanghai Chenhua Instrument Co., Ltd. was employed for catalyst testing. Photocatalytic oxygen evolution activity in water was studied using an MC-PF300B (Beijing Morison Technology Co., Ltd.).

2.2. Catalyst synthesis

2.2.1. Synthesis of MIL-101(Fe)

MIL-101(Fe) was synthesized according to previous work [36]. DMF (15 mL) was used to dissolve NH_2-H_2BDC (90.6 mg, 0.5 mmol) and $FeCl_3 \cdot 6H_2O$ (135.1mg, 0.5 mmol) under magnetic stirring for 10 mins. Then, synthesis was performed in a sealed stainless-steel reactor (20 mL volume) at 110 °C for 20 hours. Next, the reaction mixture was allowed to cool to ambient temperature, and the obtained solid brown particles underwent centrifugation and were washed with DMF and ethanol. After washing, the obtained MIL-101(Fe) was dried in an oven at 60 °C for 12 hours and then vacuum-dried at 120 °C for 8 hours.

2.2.2. Synthesis of C_3N_4 QDs

A C_3N_4 QDs solution was synthesized according to previous work [41]. First, trisodium citrate (0.81 g) and urea (1.01 g) were mixed and ground using a mortar and pestle. This mixture was added to a crucible, which was covered and heated at 180 °C for 1 hour in a muffle furnace. Methanol was used to wash the obtained dark brown QD powder 3-4 times to remove any remaining impurities, followed by drying in an oven. Next, water (10 mL) was used to disperse the dry C_3N_4 QD powder (100 mg), and dialysis was performed with a 10,000 k Da dialysis membrane. The solution after dialysis was collected and stored for subsequent use.

2.2.3. Preparation of C_3N_4 QDs/MIL-101(Fe)

A series of C_3N_4 QDs/MIL-101(Fe) was prepared using a modified version of the steps employed to obtain MIL-101(Fe). To load the C_3N_4 QDs on the MOF, 1 mL, 5 mL, or 10 mL of C_3N_4 QD solution was combined

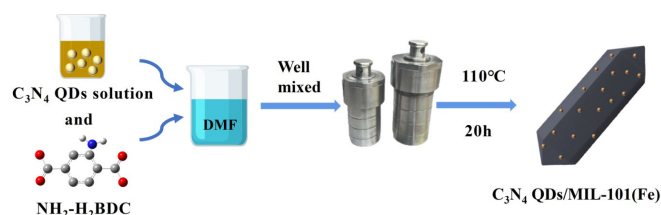


Figure 1. Catalyst preparation flow chart.

with the $FeCl_3 \cdot 6H_2O$ and NH_2-H_2BDC precursor solution. Thus, a series of composites with different C_3N_4 QD loadings were prepared, and these composites were denoted as C_3N_4 QDs/MIL-101(Fe)-1, C_3N_4 QDs/MIL-101(Fe)-5, and C_3N_4 QDs/MIL-101(Fe)-10. Figure 1 shows the material preparation process.

3. Results and Discussion

3.1. SEM and TEM examination

The MIL-101(Fe), C_3N_4 QDs/MIL-101(Fe)-1, C_3N_4 QDs/MIL-101(Fe)-5, and C_3N_4 QDs/MIL-101(Fe)-10 sample morphologies were studied using SEM and TEM. Figure 2(a) shows an SEM micrograph of MIL-101(Fe). This sample had a typical octahedral shape, smooth surface, clear edges, a uniform structure, and a uniform particle size. In comparison, as shown in Figures 2(b-d) the C_3N_4 QDs/MIL-101(Fe) composite samples had a dodecahedral spinner morphology and rougher surfaces. The addition of excessive QD solution during sample preparation led to agglomeration on the composite surface (Figure 2d), demonstrating that the addition of QDs changed the morphology of MIL-101(Fe) to some extent. The TEM image displayed in Figure 2(e) shows the uniform surface loading of C_3N_4 QDs on the MOF. At a higher resolution (Figure 2f), a C_3N_4 QDs lattice spacing of 0.34 nm was observed, in agreement with other literature reports [41]. These results confirm the successful preparation of C_3N_4 QDs/MIL-101(Fe).

3.2. XRD analysis

XRD was used to further study the prepared catalysts, as displayed in Figure 3. C_3N_4 QDs/MIL-101(Fe) and MIL-101(Fe) showed XRD peaks at $2\theta = 8.4^\circ, 9.0^\circ, 16.4^\circ,$ and 18.9° , matching the simulated MIL-101(Fe) XRD pattern and those reported in the literature [42]. No other diffraction peaks were observed, indicating that this composite photocatalytic material was highly pure and did not contain any impurities.

3.3. X-ray photoelectron spectroscopy (XPS) analysis

X-ray photoelectron spectroscopy (XPS) was employed to study the elemental states and chemical composition of C_3N_4 QDs/MIL-101(Fe)-5 (Figure 4). As shown in Figure S1, this composite catalyst contained C, N, O, and Fe. Characteristic C 1s peaks were observed at 284.8 eV (C-C bonds), 286.3 eV (C-O bonds), and 288.7 eV (C=O bonds), as shown in Figure 4(a). Characteristic O 1s peaks were observed at 530.4 eV (Fe-O bonds), 532.0 eV (C-O bonds), and 533.6 eV (C=O bonds), as shown in Figure 4(b). Characteristic N 1s peaks were observed at C 399.5 eV (C-N=C), 400.5 eV (C-N₃), and 402.3 eV (C-NH₂), as displayed in Figure 4(c). Characteristic $Fe2p_{3/2}$ and $Fe2p_{1/2}$ peaks were observed near 711.8 eV and 725.2 eV, and satellite peaks of ferric ions were located at 718.3 eV and 731.2 eV, as shown in Figure 4(d). Together with the XRD analysis, this confirmed the successful synthesis of the C_3N_4 QDs/MIL-101(Fe) composites.

3.4. Nitrogen adsorption-desorption analysis

The N_2 adsorption-desorption isotherm of each prepared sample has been displayed in Figure 5(a), and the related textural properties have been listed in Table 1. The Brunauer-Emmett-Teller (BET) specific surface areas of MIL-101(Fe), C_3N_4 QDs/MIL-101(Fe)-1, C_3N_4 QDs/MIL-101(Fe)-5, and C_3N_4 QDs/MIL-101(Fe)-10 were 60.5 m²/g, 69.5 m²/g,

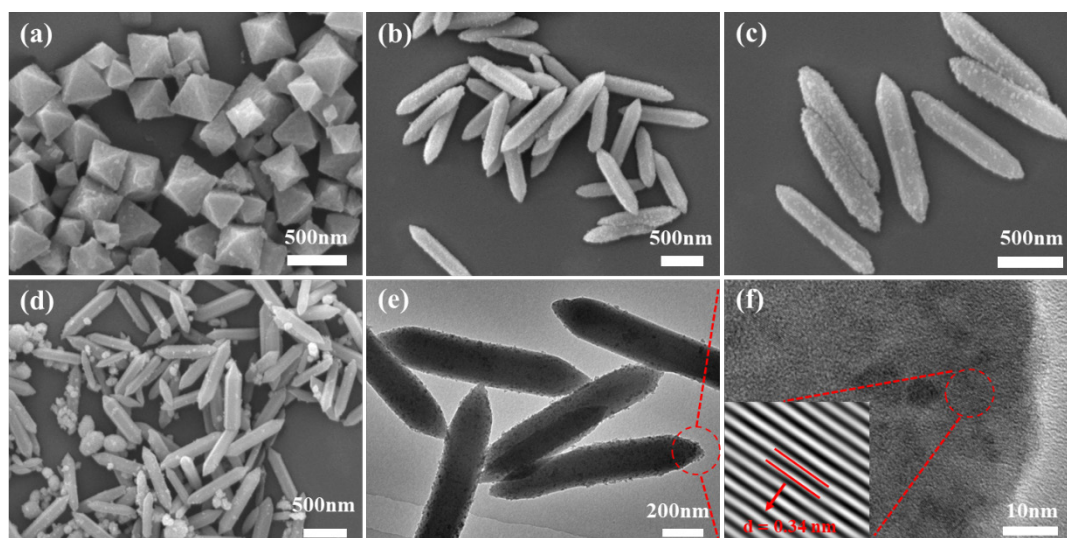


Figure 2. SEM micrographs of (a) MIL-101(Fe), (b) C_3N_4 QDs/MIL-101(Fe)-1, (c) C_3N_4 QDs/MIL-101(Fe)-5, and (d) C_3N_4 QDs/MIL-101(Fe)-10; (e) TEM and (f) high-resolution TEM micrographs of C_3N_4 QDs/MIL-101(Fe)-5. In (e), the red circle highlights a specific area of interest. In (f), the red dotted lines and red arrows indicate the lattice fringes, and the red circle marks a particular region, with the inset showing an enlarged view of the lattice structure where the interplanar spacing $d = 0.34$ nm is measured.

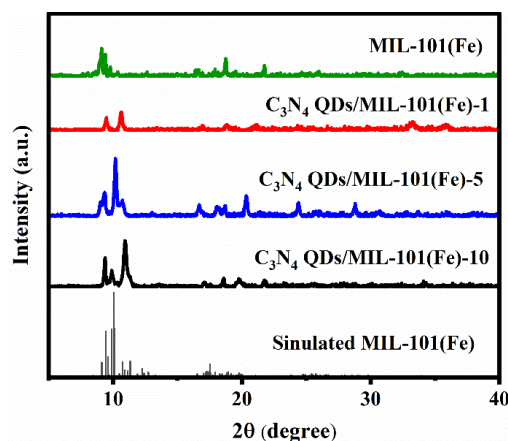


Figure 3. XRD patterns of sample catalysts.

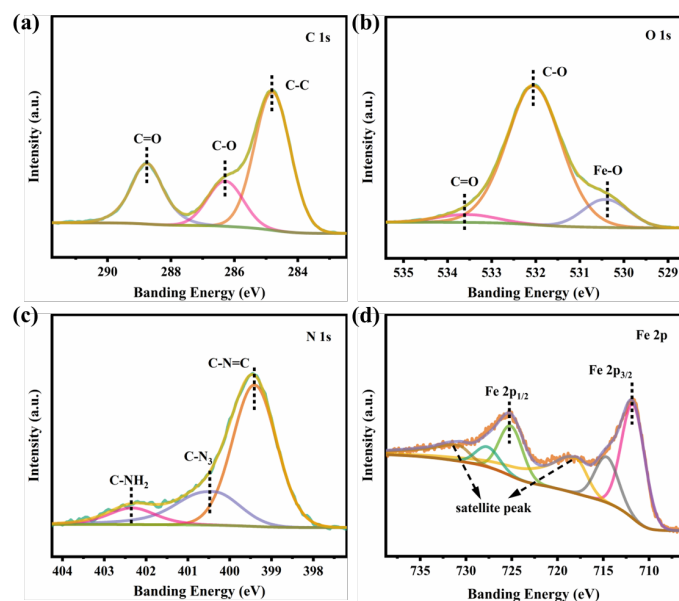


Figure 4. (a) C 1s, (b) O 1s, (c) N 1s, and (d) Fe 2p XPS spectra of C_3N_4 QDs/MIL-101(Fe)-5.

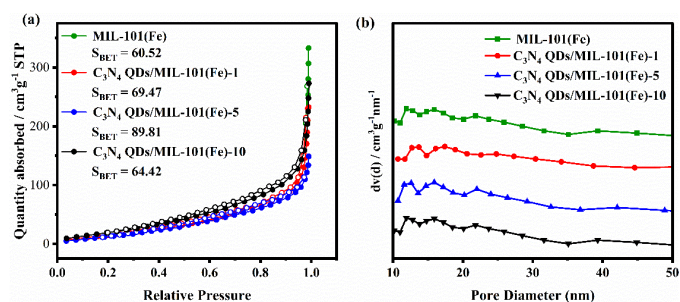


Figure 5. (a) Nitrogen adsorption-desorption and (b) pore size distributions of the prepared catalyst samples.

Table 1. Textural characteristics of the prepared catalysts.

| Catalyst | Specific surface area (m^2/g) | Pore volume (cm^3/g) | Average pore size (nm) |
|-----------------------------|-----------------------------------|--------------------------|------------------------|
| MIL-101(Fe) | 60.5 | 0.208 | 62.4 |
| C_3N_4 QDs/MIL-101(Fe)-1 | 69.5 | 0.424 | 94.5 |
| C_3N_4 QDs/MIL-101(Fe)-5 | 89.8 | 0.518 | 149.1 |
| C_3N_4 QDs/MIL-101(Fe)-10 | 64.4 | 0.232 | 71.9 |

89.8 m^2/g , and 64.4 m^2/g , respectively. Therefore, an appropriate loading of C_3N_4 QDs increased the specific surface area, while excessive loading led to the accumulation and agglomeration of C_3N_4 QDs and a subsequent decline in specific surface area. This decline in surface area was not expected to be conducive to the photocatalytic reaction. The pore size distribution of each sample catalyst was concentrated around 12 nm (Figure 5b).

3.5. Light absorption performance

The optical absorption of each prepared catalyst was evaluated using UV-vis DRS, as shown in Figure 6(a). The intersections of the tangent lines with the X-axis represent the light absorption band edge of each sample. MIL-101(Fe) had an absorption band edge of about 535.6 nm. In contrast, the composite catalysts had wider light absorption ranges, indicating that QD loading led to the more effective utilization of visible light. Formula S1 was used to calculate the band gaps of the catalysts, as shown in Figure 6(b). MIL-101(Fe), C_3N_4 QDs/MIL-101(Fe)-5, and C_3N_4 QDs/MIL-101(Fe)-10 had band gaps of 2.64 eV,

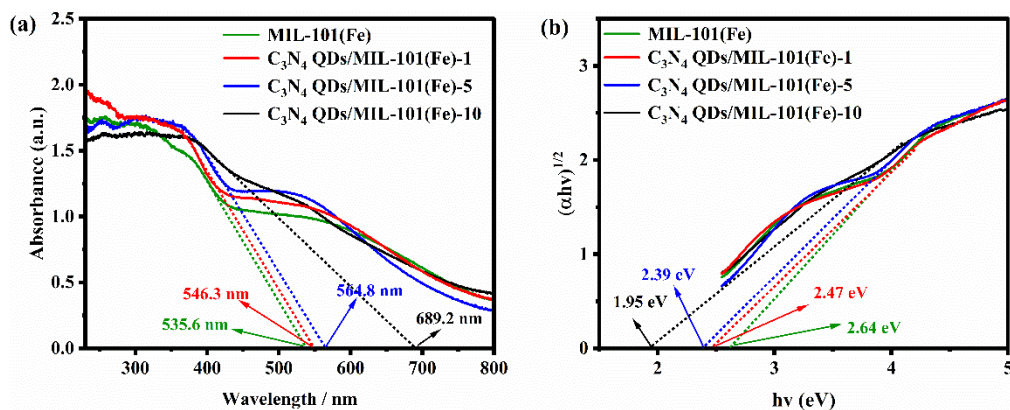


Figure 6. (a) UV-vis DRS and (b) band gap diagram of the prepared catalysts.

2.39 eV, and 1.95 eV, respectively. Thus, loading QDs reduced the band gap, indicating that less energy was required for electron transfer and that more electrons were excited. This showed good promise for achieving improved photocatalytic activity.

3.6. PL spectral analysis

Photoluminescence spectroscopy (PLS) was used to analyze the luminous intensities of the prepared catalyst samples and explore their photocatalytic activity, as shown in Figure 7. MIL-101(Fe), C_3N_4 QDs/MIL-101(Fe)-1, C_3N_4 QDs/MIL-101(Fe)-5, and C_3N_4 QDs/MIL-101(Fe)-10 all showed strong fluorescence signal peaks at about 442 nm and 475 nm. The fluorescence in intensities of the composites was lower than that of MIL-101(Fe), and C_3N_4 QDs/MIL-101(Fe)-5 exhibited the lowest fluorescence intensity. In general, weaker fluorescence properties indicate a stronger ability to separate electron-hole pairs [43]. This is conducive to inhibiting the recombination of photogenerated electron-hole pairs and enhancing the transfer of photogenerated charges, leading to better photocatalytic performance.

3.7. Photoelectric properties

The transient photocurrent response of each catalyst was determined to test the transfer and generation of photoexcited charge carriers, as shown in Figure 8(a). A stronger photocurrent intensity indicates a better electron-hole separation effect. C_3N_4 QDs/MIL-101(Fe)-5 showed a stronger photocurrent response than the other three catalysts, indicating improved charge transfer efficiency, inhibited hole-electron pair recombination, and enhanced photocatalytic activity. An impedance diagram of the four catalysts is presented in Figure 8(b). A smaller arc radius demonstrates lower resistance and improved charge transfer efficiency. The composite catalysts had smaller arc radii than MIL-101(Fe). C_3N_4 QDs/MIL-101(Fe)-5 showed the smallest radius, demonstrating the lowest charge transfer resistance and the most rapid electron transfer process. Mott-Schottky (M-S) curves of MIL-101(Fe)

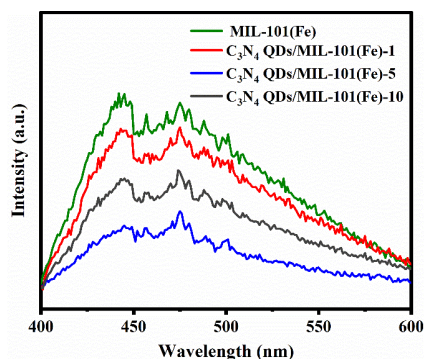


Figure 7. PL spectra of different samples.

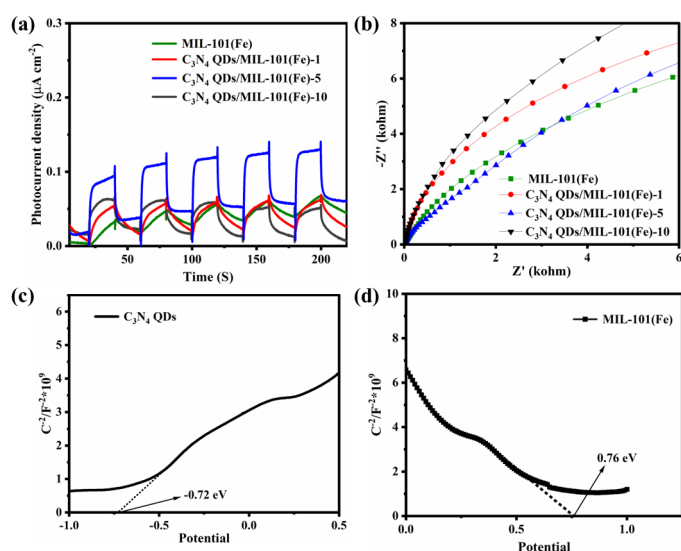


Figure 8. (a) Photocurrent intensities and (b) EIS curves of the prepared catalysts; (c) M-S curves of C_3N_4 QDs and (d) MIL-101(Fe).

and C_3N_4 QDs were obtained to determine their conduction and valence bands. According to the value of the intersection between the tangent line of the M-S curve and the X-axis in Figure 8(c), the C_3N_4 QDs had a conduction potential of -0.72 eV. Combined with the 2.7 eV band gap value of C_3N_4 QDs, the calculated valence band potential of C_3N_4 QDs was determined to be 1.98 eV. The valence band potential of MIL-101(Fe) was 0.76 eV at the intersection of the M-S curve tangent line and X-axis, as shown in Figure 8(d). Based on the 2.64 eV band gap of MIL-101(Fe), the conduction band potential of MIL-101(Fe) was determined to be -1.88 eV. In summary, these photochemical test results verify that loading C_3N_4 QDs on MIL-101(Fe) inhibited photogenerated charge carrier recombination, which provided improved migration and separation. This showed promise for achieving enhanced photodegradation activity.

3.8. Photocatalytic activity and stability

An organic pollutant was photocatalytically degraded by the synthesized catalysts using a xenon lamp light source to simulate sunlight. The performance of the prepared catalysts was evaluated by using Congo red as a model organic contaminant. As displayed in Figures 9(a) and 9(b), MIL-101(Fe) had the worst photocatalytic effect, and the Congo red degradation efficiency after 20 min of light exposure was only 72.3%. In comparison, the C_3N_4 QDs/MIL-101(Fe) composites showed significantly improved performance. C_3N_4 QDs/MIL-101(Fe)-1, C_3N_4 QDs/MIL-101(Fe)-5, and C_3N_4 QDs/MIL-101(Fe)-10 had Congo red degradation efficiencies of 93.5%, 99.5%, and 83.6%, respectively.

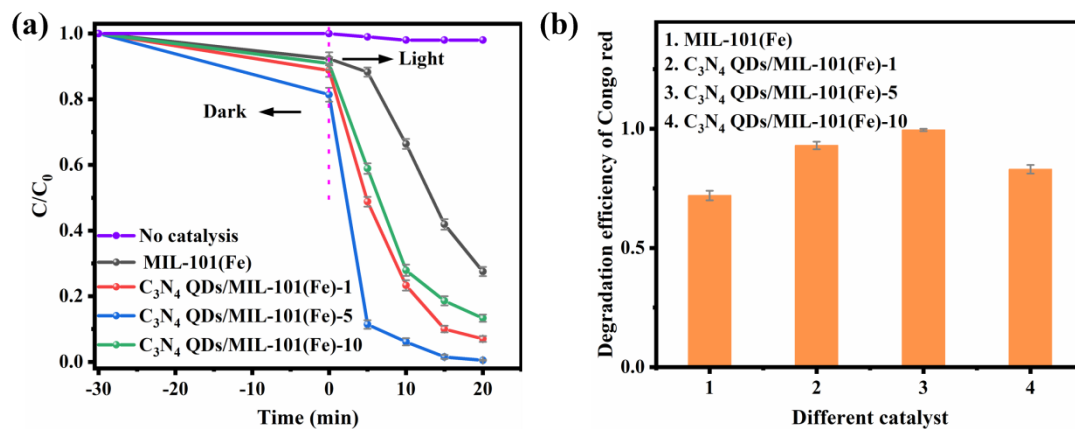


Figure 9. (a) Photodegradation of Congo red by prepared catalysts over time; (b) histogram of Congo red degradation efficiencies by the prepared catalysts.

C₃N₄ QDs/MIL-101(Fe)-5 showed the most improved photodegradation effect, followed by C₃N₄ QDs/MIL-101(Fe)-1. Meanwhile, C₃N₄ QDs/MIL-101(Fe)-10 had the worst performance among these three composite catalysts. The addition of C₃N₄ QDs enhanced visible light absorption, which generated more photogenerated electrons and holes. However, in the presence of an excessive C₃N₄ QD loading, QD agglomeration likely blocked photogenerated charge carrier migration. To probe the exact active species and identify the electron transfer mechanism, radical trapping experiments were conducted for the degradation process of the Congo red solution with C₃N₄ QDs/MIL-101(Fe)-5 composites. Na₂C₂O₄, isopropanol (IPA), and benzoquinone (BQ) were adopted as the H⁺ scavenger, ·OH quencher, and ·O₂⁻ scavenger in the trapping experiments, respectively. As shown in Figure S1, the BQ had the strongest negative effects on the degradation rate for Congo red. However, the IPA and Na₂C₂O₄ had little effect on the degradation process. These results clearly demonstrate that ·O₂⁻ species play an essential role in the Congo red photocatalytic degradation process, but the H⁺ and ·OH play a minor role.

3.9. Mechanism analysis

On this basis, the possible reaction mechanism of the prepared composite catalysts was proposed, as shown in Figure 10. The composite catalyst C₃N₄ QDs/MIL-101(Fe)-5 generates photogenerated electrons and holes under simulated sunlight, and these charge carriers are then transferred to the catalyst surface. Because the photogenerated electron-hole pairs are transferred to a low energy level, the electrons on MIL-101(Fe) are transferred to the C₃N₄ QDs, where they react with oxygen to form ·O₂⁻ free radicals. Concurrently, the holes on the C₃N₄ QDs undergo transfer to MIL-101(Fe), thereby facilitating the efficient separation of photogenerated electron-hole pairs. Nevertheless, because its valence band potential falls below the oxidation potential of OH⁻/·OH

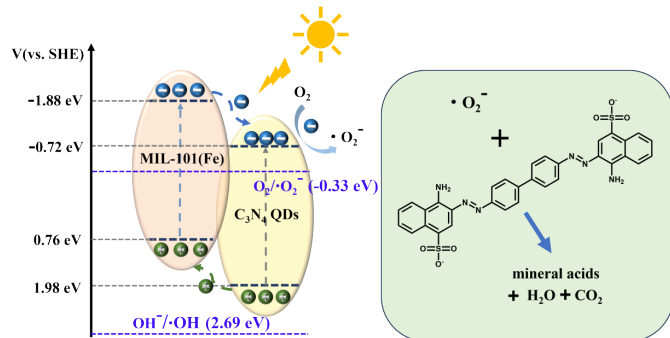


Figure 10. Mechanism of Congo red photocatalytic degradation by C₃N₄ QDs/MIL-101(Fe).

(2.69 eV), the conversion of OH⁻ into ·OH radicals remains unattainable [37]. Finally, the ·O₂⁻ radicals degrade Congo red into inorganic acids, H₂O, and CO₂.

4. Conclusions

In this study, MIL-101(Fe) and composite C₃N₄ QDs/MIL-101(Fe) catalysts were hydrothermally synthesized in the presence or absence of a C₃N₄ QD solution during synthesis. The prepared catalysts were analyzed by a range of characterization techniques, and their performance was evaluated for the photocatalytic degradation of Congo red solution. The following conclusions were obtained: improved photocatalytic performance was achieved by identifying the optimal C₃N₄ QD loading. Excessively low loading did not have a significant effect on catalytic activity, while an excessively high QD loading led to the aggregation of the C₃N₄ QDs, which negatively affected the catalytic effect. The composites had wider light adsorption ranges than MIL-101(Fe), indicating their enhanced light utilization efficiency. The composites also had larger specific surface areas than MIL-101(Fe). Moreover, the composites had lower fluorescence intensities than the unloaded MOF, favoring the effective separation of photogenerated holes and electrons. The synthesized catalysts were utilized to photocatalytically degrade 100 mg/L Congo red solution. C₃N₄ QDs/MIL-101(Fe)-5 had the best degradation performance. After 20 mins, this catalyst had a 99.5% Congo red degradation efficiency, which was 1.38 times higher than that of MIL-101(Fe). To summarize, compared with MIL-101(Fe), C₃N₄ QDs/MIL-101(Fe) inhibited electron hole-pair recombination, leading to the enhanced migration and separation of electrons and holes. This led to significantly improved photocatalytic performance. These composite catalysts show broad application prospects for the photocatalytic degradation of organic pollutants.

Data availability statement

The datasets used and/or analyzed during the current study available from the corresponding author on reasonable request.

CRediT authorship contribution statement

Changbo Zhang contributed to the conception of the study and design of methodology; Shunshun Yu and Liang Wu performed the experiment; Tong Lv and Keliang Wu performed the data analyses and wrote the manuscript, Bingke Li and Junjie Bai act as visualization.

Declaration of competing interest

The authors declare that they have no known competing financial interests or personal relationships that could have appeared to influence the work reported in this paper.

Declaration of Generative AI and AI-assisted technologies in the writing process

The authors confirm that there was no use of artificial intelligence (AI)-assisted technology for assisting in the writing or editing of the manuscript and no images were manipulated using AI.

Acknowledgements

The authors disclosed receipt of the following financial support for the research, authorship, and publication of this article: This work was supported by Guizhou Provincial Science and Technology Projects (Grant No. QiankeheFoundation- [2024] Youth412) and Scientific Research Foundation for Projects of Minzu Normal University of Xingyi (Grant Nos. 21XYBS13, 21XYZD05) and Henan Sikruining Biopharmaceutical R&D Co., Ltd School-Enterprise Cooperation Project (202403150735).

Supplementary data

Supplemental data can be found online at https://dx.doi.org/10.25259/AJC_296_2024.

References

- Gong, P., Xu, H., Wang, C., Chen, Y., Guo, L., Wang, X., 2021. Persistent organic pollutant cycling in forests. *Nature Reviews Earth & Environment*, **2**, 182-197. <https://doi.org/10.1038/s43017-020-00137-5>
- Rojas, S., Horcajada, P., 2020. Metal-organic frameworks for the removal of emerging organic contaminants in water. *Chemical Reviews*, **120**, 8378-8415. <https://doi.org/10.1021/acs.chemrev.9b00797>
- Skorjanc, T., Shetty, D., Trabolsi, A., 2021. Pollutant removal with organic macrocycle-based covalent organic polymers and frameworks. *Chemical*, **7**, 882-918. <https://doi.org/10.1016/j.chempr.2021.01.002>
- Chen, Z., Lu, Y.L., Wang, L., Xu, J., Zhang, J., Xu, X., Cheng, P., Yang, S., Shi, W., 2023. Efficient recognition and removal of persistent organic pollutants by a bifunctional molecular material. *Journal of the American Chemical Society*, **145**, 260-267. <https://doi.org/10.1021/jacs.2c09866>
- Wang, X., Ren, L., Long, T., Geng, C., Tian, X., 2023. Migration and remediation of organic liquid pollutants in porous soils and sedimentary rocks: A review. *Environmental Chemistry Letters*, **21**, 479-496. <https://doi.org/10.1007/s10311-022-01506-w>
- Grandclément, C., Seyssiecq, I., Piram, A., Wong-Wah-Chung, P., Vanot, G., Tiliacos, N., Roche, N., Doumenq, P., 2017. From the conventional biological wastewater treatment to hybrid processes, the evaluation of organic micropollutant removal: A review. *Water Research*, **111**, 297-317. <https://doi.org/10.1016/j.watres.2017.01.005>
- Jain, B., Singh, A.K., Kim, H., Lichtfouse, E., Sharma, V.K., 2018. Treatment of organic pollutants by homogeneous and heterogeneous Fenton reaction processes. *Environmental Chemistry Letters*, **16**, 947-967. <https://doi.org/10.1007/s10311-018-0738-3>
- Morin-Crini, N., Lichtfouse, E., Fourmentin, M., Ribeiro, A.R.L., Noutsopoulos, C., Mapelli, F., Fenyvesi, É., Vieira, M.G.A., Picos-Corrales, L.A., Moreno-Piraján, J.C., Giraldo, L., Sohajda, T., Huq, M.M., Soltan, J., Torri, G., Magureanu, M., Bradu, C., Crini, G., 2022. Removal of emerging contaminants from wastewater using advanced treatments. A review. *Environmental Chemistry Letters*, **20**, 1333-1375. <https://doi.org/10.1007/s10311-021-01379-5>
- Gusain, R., Gupta, K., Joshi, P., Khatri, O.P., 2019. Adsorptive removal and photocatalytic degradation of organic pollutants using metal oxides and their composites: A comprehensive review. *Advances in Colloid and Interface Science*, **272**, 102009. <https://doi.org/10.1016/j.cis.2019.102009>
- Silvestri, S., Fajardo, A., Iglesias, B.A., 2022. Supported porphyrins for the photocatalytic degradation of organic contaminants in water: A review. *Environmental Chemistry Letters*, **20**, 731-771. <https://doi.org/10.1007/s10311-021-01344-2>
- Wang, C.-C., Li, J.-R., Lv, X.-L., Zhang, Y.-Q., Guo, G., 2014. Photocatalytic organic pollutants degradation in metal-organic frameworks. *Energy & Environmental Science*, **7**, 2831-2867. <https://doi.org/10.1039/c4ee01299b>
- El-Bindary, A.A., El-Marsafy, S.M., El-Maddah, A.A., 2019. Enhancement of the photocatalytic activity of ZnO nanoparticles by silver doping for the degradation of AY99 contaminants. *Journal of Molecular Structure*, **1191**, 76-84. <https://doi.org/10.1016/j.molstruc.2019.04.064>
- Kiwaan, H.A., Atwee, T.M., Azab, E.A., El-Bindary, A.A., 2020. Photocatalytic degradation of organic dyes in the presence of nanostructured titanium dioxide. *Journal of Molecular Structure*, **1200**, 127115. <https://doi.org/10.1016/j.molstruc.2019.127115>
- El-Dossoki, F.I., Atwee, T.M., Hamada, A.M., El-Bindary, A.A., 2021. Photocatalytic degradation of remazol red B and rhodamine B dyes using TiO₂ nanomaterial: Estimation of the effective operating parameters. *Desalination and Water Treatment*, **233**, 319-330. <https://doi.org/10.5004/dwt.2021.27519>
- Kiwaan, H.A., Atwee, T.M., Azab, E.A., El-Bindary, A.A., 2019. Efficient photocatalytic degradation of Acid Red 57 using synthesized ZnO nanowires. *Journal of the Chinese Chemical Society*, **66**, 89-98. <https://doi.org/10.1002/jccs.201800092>
- Awad, M.E., Farrag, A.M., El-Bindary, A.A., El-Bindary, M.A., Kiwaan, H.A., 2023. Photocatalytic degradation of Rhodamine B dye using low-cost pyrofabricated titanium dioxide quantum dots-kaolinite nanocomposite. *Applied Organometallic Chemistry*, **37**, e7113. <https://doi.org/10.1002/aoc.7113>
- Awad, M.E., Farrag, A.M., Aboelnga M.M., El-Bindary A.A., 2025. Optimization of photocatalytic degradation of rhodamine B and indigo carmine dyes using eco-friendly kaolinite-silver oxide quantum dots nanocomposite under sunlight irradiation. *Applied Organometallic Chemistry*, **39**, e7842. <https://doi.org/10.1002/aoc.7842>
- El-Bindary, A.A., Beheary, M.S., Samra, N.S., Adly, M.S., 2022. Enhanced photocatalytic degradation of methylene blue dye under UV-light irradiation using Bi₂S₃/ZnS and ZnS/Bi₂S₃ nanocomposites. *Egyptian Journal of Chemistry*, **66**, 293-306. <https://doi.org/10.21608/ejchem.2022.173941.7212>
- Chen, C., Fei, L., Wang, B., Xu, J., Li, B., Shen, L., Lin, H., 2024. MOF-based photocatalytic membrane for water purification: A review. *Small (Weinheim an der Bergstrasse, Germany)*, **20**, e2305066. <https://doi.org/10.1002/smll.202305066>
- Ju, Y., Wang, Z., Lin, H., Hou, R., Li, H., Wang, Z., Zhi, R., Lu, X., Tang, Y., Chen, F., 2024. Modulating the microenvironment of catalytic interface with functional groups for efficient photocatalytic degradation of persistent organic pollutants. *Chemical Engineering Journal*, **479**, 147800. <https://doi.org/10.1016/j.cej.2023.147800>
- Zheng, Z., Tian, S., Feng, Y., Zhao, S., Li, X., Wang, S., He, Z., 2023. Recent advances of photocatalytic coupling technologies for wastewater treatment. *Chinese Journal of Catalysis*, **54**, 88-136. [https://doi.org/10.1016/s1872-2067\(23\)64536-x](https://doi.org/10.1016/s1872-2067(23)64536-x)
- Hussain, M.Z., Yang, Z., Huang, Z., Jia, Q., Zhu, Y., Xia, Y., 2021. Recent advances in metal-organic frameworks derived nanocomposites for photocatalytic applications in energy and environment. *Advanced Science*, **8**, 2100625. <https://doi.org/10.1002/advs.202100625>
- Qian, Y.T., Zhang, F.F., Pang, H., 2021. A review of MOFs and their composites-based photocatalysts: Synthesis and applications. *Advanced Functional Materials*, **31**, 2104231. <https://doi.org/10.1002/adfm.202104231>
- Zhang, X., Tong, S., Huang, D., Liu, Z., Shao, B., Liang, Q., Wu, T., Pan, Y., Huang, J., Liu, Y., Cheng, M., Chen, M., 2021. Recent advances of Zr based metal organic frameworks photocatalysis: Energy production and environmental remediation. *Coordination Chemistry Reviews*, **448**, 214177. <https://doi.org/10.1016/j.ccr.2021.214177>
- Chen, J., Qin, C., Mou, Y., Cao, Y., Chen, H., Yuan, X., Wang, H., 2023. Linker regulation of iron-based MOFs for highly effective Fenton-like degradation of refractory organic contaminants. *Chemical Engineering Journal*, **459**, 141588. <https://doi.org/10.1016/j.cej.2023.141588>
- Lv, S.-W., Cong, Y., Chen, X., Wang, W., Che, L., 2022. Developing fine-tuned metal-organic frameworks for photocatalytic treatment of wastewater: A review. *Chemical Engineering Journal*, **433**, 133605. <https://doi.org/10.1016/j.cej.2021.133605>
- Sun, P., Xing, Z., Li, Z., Zhou, W., 2023. Recent advances in quantum dots photocatalysts. *Chemical Engineering Journal*, **458**, 141399. <https://doi.org/10.1016/j.cej.2023.141399>
- Wang, R., Lu, K.-Q., Tang, Z.-R., Xu, Y.-J., 2017. Recent progress in carbon quantum dots: Synthesis, properties and applications in photocatalysis. *Journal of Materials Chemistry A*, **5**, 3717-3734. <https://doi.org/10.1039/c6ta08660h>
- Wang, X., Sun, G., Li, N., Chen, P., 2016. Quantum dots derived from two-dimensional materials and their applications for catalysis and energy. *Chemical Society Reviews*, **45**, 2239-2262. <https://doi.org/10.1039/c5cs00811e>
- Feng, C., Zhang, X., Jin, H., Du, R., Wang, Y., Zhou, Y., Chong, R., Liu, X., Huang, Q., 2023. Integrating carbon vacancy modified carbon quantum dots with carbon nitride for efficient photocatalytic CO₂ reduction to syngas with tunable hydrogen to carbon monoxide ratio. *Carbon*, **203**, 671-685. <https://doi.org/10.1016/j.carbon.2022.12.021>
- Li, Q., Shen, P., Tian, Y., Li, X., Chu, K., 2022. Metal-free BN quantum dots/graphitic C₃N₄ heterostructure for nitrogen reduction reaction. *Journal of Colloid and Interface Science*, **606**, 204-212. <https://doi.org/10.1016/j.jcis.2021.08.032>
- Ma, P., Zhang, X., Wang, C., Wang, Z., Wang, K., Feng, Y., Wang, J., Zhai, Y., Deng, J., Wang, L., Zheng, K., 2022. Band alignment of homojunction by anchoring CN quantum dots on g-C₃N₄ (0D/2D) enhance photocatalytic hydrogen peroxide evolution. *Applied Catalysis B: Environmental*, **300**, 120736. <https://doi.org/10.1016/j.apcatb.2021.120736>
- J. Pan, Z. Dong, Z. Jiang, C. Zhao, B. Wang, W. Zhao, J. Wang, C. Song, Y. Zheng, C. Li, 2019. MoS₂ quantum dots modified black Ti³⁺-TiO₂/g-C₃N₄ hollow nanosphere heterojunction toward photocatalytic hydrogen production enhancement. *Solar RRL*, **3**, 1900337. <https://doi.org/10.1002/solr.201900337>
- Truong, H.B., Huy, B.T., Ray, S.K., Lee, Y.-I., Cho, J., Hur, J., 2021. Visible light-activated NGQD/nC₃N₄/Bi₂WO₆ microsphere composite for effluent organic matter treatment. *Chemical Engineering Journal*, **415**, 129024. <https://doi.org/10.1016/j.cej.2021.129024>
- Wang, W., Fang, J., Chen, H., Bao, N., Lu, C., 2019. Rice-husk-derived mesoporous 0D/2D C₃N₄ isotope heterojunction with improved quantum effect for photodegradation of tetracycline antibiotics. *Ceramics International*, **45**, 2234-2240. <https://doi.org/10.1016/j.ceramint.2018.10.136>
- Peng, B., Yang, D., Li, Z., Yuan, H., Wu, P., Huang, K., Sun, K., Zhu, J., Wu, K., Liu, Z., 2024. Iron-based nanoporous metal-organic frameworks with side-chain amino substituents for efficiency-regulated oxygen evolution reaction. *Journal of Industrial and Engineering Chemistry*, **136**, 341-348. <https://doi.org/10.1016/j.jiec.2024.02.022>
- Jiang, Y., Gao, B., Wang, Z., Li, J., Du, Y., He, C., Liu, Y., Yao, G., Lai, B., 2023. Efficient wastewater disinfection by raised 1O₂ yield through enhanced electron

- transfer and intersystem crossing via photocatalysis of peroxymonosulfate with CuS quantum dots modified MIL-101(Fe). *Water Research*, **229**, 119489. <https://doi.org/10.1016/j.watres.2022.119489>
38. Jiang, Y., Wang, Z., Huang, J., Yan, F., Du, Y., He, C., Liu, Y., Yao, G., Lai, B., 2022. A singlet oxygen dominated process through photocatalysis of CuS-modified MIL-101(Fe) assisted by peroxymonosulfate for efficient water disinfection. *Chemical Engineering Journal*, **439**, 135788. <https://doi.org/10.1016/j.cej.2022.135788>
39. Zorainy, M.Y., Gar Alalm, M., Kaliaguine, S., Boffito, D.C., 2021. Revisiting the MIL-101 metal-organic framework: Design, synthesis, modifications, advances, and recent applications. *Journal of Materials Chemistry A*, **9**, 22159-22217. <https://doi.org/10.1039/d1ta06238g>
40. Zhao, F., Liu, Y., Hammouda, S.B., Doshi, B., Guijarro, N., Min, X., Tang, C.-J., Sillanpää, M., Sivula, K., Wang, S., 2020. MIL-101(Fe)/g-C₃N₄ for enhanced visible-light-driven photocatalysis toward simultaneous reduction of Cr(VI) and oxidation of bisphenol A in aqueous media. *Applied Catalysis B: Environmental*, **272**, 119033. <https://doi.org/10.1016/j.apcatb.2020.119033>
41. Zhou, J., Yang, Y., Zhang, C.Y., 2013. A low-temperature solid-phase method to synthesize highly fluorescent carbon nitride dots with tunable emission. *Chemical communications (Cambridge, England)*, **49**, 8605-8607. <https://doi.org/10.1039/c3cc42266f>
42. Gomes Silva, C., Luz, I., Llabrés i Xamena, F.X., Corma, A., García, H., 2010. Water stable Zr-benzenedicarboxylate metal-organic frameworks as photocatalysts for hydrogen generation. *Chemistry (Weinheim an der Bergstrasse, Germany)*, **16**, 11133-11138. <https://doi.org/10.1002/chem.200903526>
43. Fang, Y., Xu, Y., Li, X., Ma, Y., Wang, X., 2018. Coating polymeric carbon nitride photoanodes on conductive Y:ZnO nanorod arrays for overall water splitting. *Angewandte Chemie (International ed. in English)*, **57**, 9749-9753. <https://doi.org/10.1002/anie.201804530>